# Use of hybrid phenomenological and statistical effective-medium theories of dielectric functions to model the infrared reflectance of porous SiC films

Jonathan E. Spanier and Irving P. Herman
*Department of Applied Physics and the Columbia Radiation Laboratory, Columbia University, New York, New York 10027*
(Received 5 May 1999; revised manuscript received 18 August 1999)

The reflectance of porous silicon carbide (PSC) thin films on SiC substrates is measured in the infrared reststrahlen region by Fourier transform infrared reflectance spectroscopy and is compared to simulated spectra based on phenomenological and Bergman statistical effective-medium dielectric functions. The phenomenological models evaluated include the Bruggeman, cavity- and sphere-Maxwell-Garnett (C-MG and S-MG), Landau-Lifshitz/Looyenga (LLL), and Monecke models. In addition, modifications to the Bruggeman and C-MG models with variable particle shapes and surface layers are examined. Hybrid versions of the C-MG and LLL models are also considered, alternatively by using a phenomenological mixing approach, which gives a direct physical interpretation of the topology, and by directly mixing the statistical spectral density functions of the C-MG and LLL effective dielectric functions. This latter statistical hybrid model gives the best (and quite good) agreement with experiments. The differences in the hybrid models are understood by comparing their spectral density functions. The dip (or splitting) in the PSC film reststrahlen band is attributed to surface optical phonon modes.

## I. INTRODUCTION

Evaluation of the dielectric function is central to understanding frequency-dependent transport, electronic and optical properties of materials, in general. It is of particular interest in studying inhomogeneous dielectric mixtures with structure having dimensions small compared to the wavelength. Dielectric functions obtained from experiment can, in fact, give insight into the nanostructure of the material. The effective-medium theory used to describe the dielectric function must be valid for, as well as account for, the macroscopic volume fractions, the local microstructural geometry of the individual materials (sizes and shapes of the constituent materials), and the microstructural topology of the mixture (how the substances are mixed and the correlation length). This paper analyzes the dielectric function of porous silicon carbide (PSC) using infrared spectroscopic data and several effective-medium theories, including a range of phenomenological models and statistical theories. It is found that a more complex treatment of the mean-field dielectric function of PSC is needed than was used in earlier treatments,[1] one that uses phenomenological and statistical mixing of the features of current models to produce new hybrid models.

Porous silicon carbide formed by anodization has been of interest in recent years because it luminesces efficiently, and more efficiently than bulk SiC.[2] A thermally grown oxide film on the pore walls further enhances the luminescence efficiency and shortens the emission wavelength of PSC.[2] Electroluminescent devices based on PSC have been demonstrated[3] and PSC has been used as a sensing material in capacitive gas sensors.[4] Devices using PSC offer advantages over those based on porous silicon due, in part, to their better mechanical and thermal stability. The much slower oxidation rate of PSC also offers the possibility of studying Si-based porous materials under better controlled conditions.

Fourier transform infrared (FTIR) reflectance has been used to investigate the infrared properties of SiC and PSC,[1,5,6] and Raman scattering spectroscopy has been used to evaluate the optical phonon spectra of PSC.[7] As a partially ionic lattice, SiC has nondegenerate longitudinal optical (LO) and transverse optical (TO) phonons in the midinfrared, and the infrared (IR) spectrum of bulk SiC has a broad reststrahlen band between the TO (793.9 $cm^{-1}$) and LO (970.1 $cm^{-1}$) phonon frequencies. Reference 1 has shown that the reststrahlen band in PSC is substantially different from that for bulk SiC in that it also has a pronounced peak at 970 $cm^{-1}$. While the simulations of IR spectra using the Maxwell-Garnett (MG) effective-medium theory presented in Ref. 1 clearly predict this feature, they do not predict the shape of the reststrahlen band in PSC, nor the dependence of this band profile on film porosity and film thickness.

In Sec. II, the procedure for preparing the PSC films is presented. In Sec. III, experimental infrared reflectance spectra are presented of as-anodized PSC using *p*-type 6H polytype and *n*-type 4H polytype starting materials. In Sec. IV, the infrared reflectance spectra of as-anodized PSC films are compared to simulations based on several effective-medium models of the dielectric function. In Sec. V, the performance of these models is evaluated and the origin of the splitting of the reststrahlen band is discussed. Concluding remarks are presented in Sec. VI.

## II. EXPERIMENTAL PROCEDURE

Two PSC films were fabricated from bulk, *p*-type 6H-SiC substrates (PSC1 and PSC2), and one from an *n*-type 4H-SiC substrate (PSC3) with $N_{A,D} \approx 10^{17} - 10^{18}\,cm^{-3}$ (Table I). Metal films were sputtered onto small areas of the substrates for contact, and the samples were encapsulated in black wax, exposing a small polished area. The $(000\overline{1})$ faces of the samples were anodized galvanostatically in a dilute ethanolic hydrofluoric acid solution for different lengths of time.

Ethanol was added to the HF solution to decrease the capillary forces which inhibit the flow of the electrolyte into

 ©2000 The American Physical Society

TABLE I. Properties of the PSC films.

| Sample | Substrate type | Doping ($cm^{-3}$) | Thickness ($\mu$m) | Porosity |
|---|---|---|---|---|
| PSC1 | *p*-type | $2.0\times10^{18}$ | 2.02 | 0.74 |
| PSC2 | *p*-type | $2.0\times10^{18}$ | 30.9 | 0.74 |
| PSC3 | *n*-type | $2.7\times10^{18}$ | 45.0 | 0.50 |

the pores. The HF and ethanol were of semiconductor and reagent grade, respectively, and the water was distilled. The films were prepared using an EG&G Model 362 scanning potentiostat. The electrolyte bath was recirculated during the anodizations to reduce the adhesion of CO, $CO_2$, and $O_2$ bubbles that evolve on the surface of the electrode and to dissipate heat. Following anodization, each sample was rinsed in ethanol and dried in air.

The PSC film thickness was determined by cross-section scanning electron microscopy (SEM) and optical microscopy. Film porosity was determined by IR reflectance interferometry. References 8–11 have been used to relate the measured optical indices of refraction and the porosities of porous silicon films in nonresonant spectral regions using several effective-medium theories. The approach of Refs. 9 and 10 was chosen here because it seems the best suited to porous materials.[12] Values of the porosity for each of the PSC films were determined by matching the model reflectance (using the measured film thickness and dielectric function effective-medium model) to the observed interference fringes in a nonresonant region of the IR reflectance spectrum. The thickness and porosity of the three PSC samples are given in Table I.

The FTIR reflectance spectra of these PSC layers in the reststrahlen and nonresonant regions were acquired using a Perkin-Elmer Paragon Model 1500 FTIR spectrometer using a specular reflectance accessory. The unpolarized reflectance was measured from 400–4000 $cm^{-1}$ at an angle of 15° with respect to the normal (the minimum angle permitted by the instrument). The resolution of the spectrometer was set at 1 $cm^{-1}$. Multiple scans were taken for each sample to ensure repeatability, and weak apodization was used. Each of the samples was cleaved or cut using a diamond saw for cross-section film thickness measurements. PSC1 will be called a ''thin'' film, and PSC2 and PSC3 will be called ''thick'' films.

## III. EXPERIMENTAL RESULTS

Figure 1(a) shows the IR spectra in the reststrahlen region of thin (PSC1) and thick (PSC2), highly porous (porosity $f=0.74$) *p*-PSC films on bulk 6H-SiC substrates, the corresponding bare bulk 6H-SiC substrate, and a thick, moderately porous ($f=0.50$) *n*-PSC film on a bulk 4H-SiC substrate (PSC3). (The IR reflectance from the 4H-SiC substrate is nearly identical to that from the 6H substrate.) Figure 1(b) shows the reflectance of the PSC films at higher energies, each of which exhibits interference fringes in the spectral region from 1000 to 4000 $cm^{-1}$. As seen in Fig. 1(a), the spectra of the *p*-PSC and *n*-PSC films are very different from that of bulk SiC. The reflectance of PSC in the SiC reststrahlen region shows a splitting of the SiC reststrahlen band

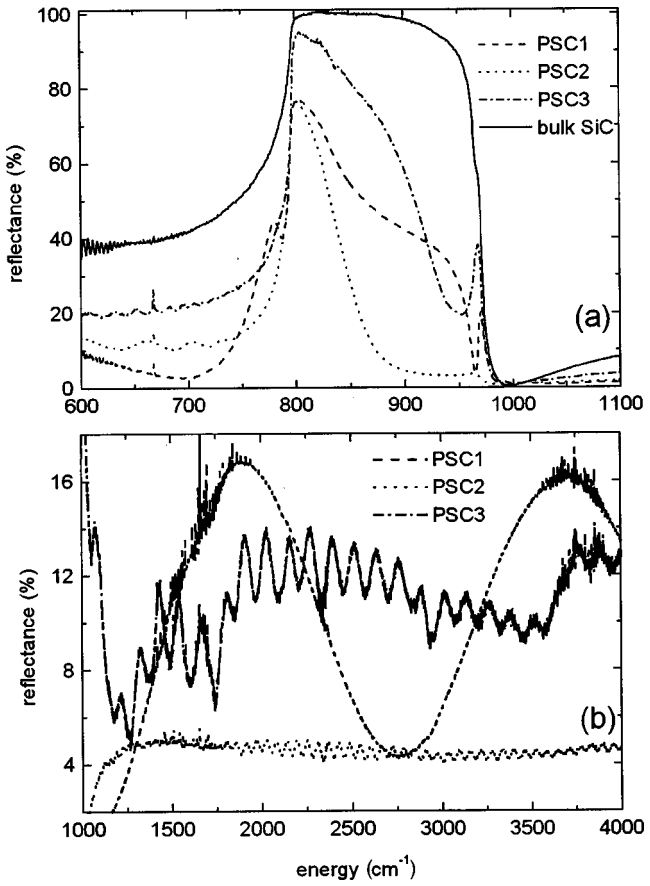


FIG. 1. Infrared reflectance (a) in the reststrahlen band from three PSC films (PSC1, PSC2, and PSC3), each on a SiC substrate, along with the IR reflectance from a bare 6H-SiC substrate, and (b) above the reststrahlen band, showing fringes due to interference in the films.

into two bands: a broad band at lower frequency (LF) and a sharp higher-frequency (HF) band near the LO frequency. While the low-frequency shoulder of the LF band in PSC is similar to that of the bulk, the high-frequency shoulder of this band has a more gradual ''descent.'' This dip in the reststrahlen band near 950–960 $cm^{-1}$ is seen in all PSC samples.

The width and shape of the reststrahlen band of PSC films of finite thickness depend on the porosity of the PSC film, as suggested in Ref. 1, but they also depend to some extent on the film thickness. Transmission electron microscopy has shown that for *p*-PSC prepared with current density $J \leqslant 30\,mA/cm^2$, higher $J$ leads to a more porous film.[2] The width and position of the shoulder of the LF reststrahlen features are observed here to depend on the formation current density and etching time (which together determine the porosity, porosity depth profile, and film thickness). Specifically, the longer the etching time (and correspondingly the thicker the porous layer) or the higher the formation current density, the more narrow the LF reststrahlen feature.

## IV. ANALYSIS

The dielectric function for bulk SiC can be modeled as a Lorentz oscillator with plasmon damping

$$\epsilon_{\mathrm{SiC}}(\omega)=\epsilon_{\infty}\left(\frac{\omega^2-\omega_L^2+i\gamma\omega}{\omega^2-\omega_T^2+i\gamma\omega}-\frac{\omega_p^2}{\omega^2+i\omega\Gamma}\right), \tag{1}$$

where $\omega_L$ and $\omega_T$ are the LO and TO phonon frequencies, $\epsilon_\infty$ is the high-frequency dielectric constant, $\gamma$ is the phonon damping parameter (4.763 $\mathrm{cm}^{-1}$,[13] unless otherwise specified), $\omega_p$ is the plasma frequency, and $\Gamma$ is the plasmon damping parameter. The second term in the parentheses describes plasmon damping and it should not affect the reststrahlen region for the low-to-moderate doping levels ($N_{A,D}\sim(2-3)\times10^{18}\,\mathrm{cm}^{-3}$, $\omega_p\ll\omega_{L,T}$) used here.

The Maxwell-Garnett (MG),[14] Bruggeman [or effective-medium approximation (EMA)],[8] Landau-Lifshitz/Looyenga (LLL),[9,10] Monecke,[15] and generalized statistical (Bergman representation)[16] effective-medium theories are used to model the dielectric function, and in turn the IR reflectance of PSC. The four phenomenological models are special analytical cases of the statistical theory. The PSC layer is modeled as a finite layer on an infinite half-space of bulk SiC. Porous silicon carbide itself is modeled as an isotropic two-phase medium consisting of bulk SiC and pores (air) for each of the three models. Bulk SiC is modeled as a Lorentzian oscillator [Eq. (1)], with the second term ignored. Modifications to the cavity-Maxwell-Garnett (C-MG) and Bruggeman models are also considered in Sec. IV C, including the effect of varying the shape of the pores and the possibility of including a third phase, an inner surface layer of SiC with different properties from the bulk SiC phase. Phenomenological hybrid models that combine effective-medium theories are considered in Sec. IV F. The generalized statistical theory of the dielectric functions is also applied, including a statistical hybrid model, in Sec. IV G. The Appendix details how the structures are modeled optically to obtain the reflectance.

The two most commonly used effective-medium models are the Maxwell-Garnett[14] and the Bruggeman[8] theories. In both, the effective dielectric function $\epsilon_{\mathrm{eff}}$ of the medium is obtained by averaging the dielectric function in each cell in the medium $\epsilon_i$, assuming that each cell is embedded in a homogeneous medium with dielectric function $\epsilon_0$. The effective dielectric function is given by

$$\epsilon_{\mathrm{eff}}(\epsilon_0)=\frac{\Sigma_i P(\epsilon_i,\epsilon_0)D(\epsilon_i,\epsilon_0)d\epsilon_i}{\Sigma_i P(\epsilon_i,\epsilon_0)E(\epsilon_i,\epsilon_0)d\epsilon_i}, \tag{2}$$

where $P$, $D$, and $E$ are the dielectric function probability distribution, the displacement vector, and the electric field, respectively. For spherical cells this reduces to the Clausius-Mossotti equation

$$\epsilon_{\mathrm{eff}}=\epsilon_0\left(\frac{1+2\langle\alpha\rangle}{1-2\langle\alpha\rangle}\right), \tag{3}$$

where $\alpha$ is the polarizability per unit cell volume

$$\alpha(\epsilon_i)=\frac{\epsilon_i-\epsilon_0}{\epsilon_i+2\epsilon_0}, \tag{4}$$

and $\langle\alpha\rangle$ denotes the average of $\alpha$ taken over all cells.

$$\langle\alpha\rangle=\left\langle\frac{\epsilon_i-\epsilon_0}{\epsilon_i+2\epsilon_0}\right\rangle=\sum_i\frac{\epsilon_i-\epsilon_0}{\epsilon_i+2\epsilon_0}f_i, \tag{5}$$

where $f_i$ is the respective volume fraction of the medium.

### A. Bruggeman theory

The Bruggeman theory imposes the self-consistent requirement $\epsilon_{\mathrm{eff}}(\epsilon_0)=\epsilon_0$. Equation (3) shows that this means $\langle\alpha\rangle=0$. For a binary disordered material consisting of two materials having dielectric functions $\epsilon_1(\omega)$ and $\epsilon_2(\omega)$, with concentrations (volume fractions) $f_1$ and $f_2$, respectively, Eq. (5) becomes

$$\left(\frac{\epsilon_1-\epsilon_{\mathrm{eff}}}{\epsilon_1+2\epsilon_{\mathrm{eff}}}\right)f_1+\left(\frac{\epsilon_2-\epsilon_{\mathrm{eff}}}{\epsilon_2+2\epsilon_{\mathrm{eff}}}\right)f_2=0. \tag{6}$$

$\epsilon_{\mathrm{eff}}(\omega)$ is explicitly given in Ref. 17. The Bruggeman model is symmetric with respect to the constituent materials; here SiC and air are both embedded in an effective medium. Equation (6) is valid only for $0.05<|\epsilon_2(\omega)/\epsilon_1(\omega)|<20$, where the fluctuations in the local value of $\epsilon_i$ are not too large.[17]

Figure 2 compares the simulated (dashed lines) and measured (solid lines) IR reflectance spectra for PSC1, PSC2, and PSC3. Although the Bruggeman model does produce a splitting of the reststrahlen band for the thin *p*-PSC (PSC1), the agreement with the measured spectrum is poor. Agreement is poor for the thicker porous layers (PSC2 and PSC3) and, in fact, the modeled reststrahlen band does not split for PSC3.

### B. Maxwell-Garnett theory

The Maxwell-Garnett theory models a binary disordered material composed of materials $A$ and $B$ with volume fractions $f_A$ and $f_B$, in the limit of small volume fraction of $A$ ($f_A\leqslant0.15$), assuming $\epsilon_0\cong\epsilon_B$. Equation (5) then gives

$$\left\langle\frac{\epsilon_i-\epsilon_0}{\epsilon_i+2\epsilon_0}\right\rangle=\left(\frac{\epsilon_A-\epsilon_B}{\epsilon_A+2\epsilon_B}\right)f_A. \tag{7}$$

Using this in Eq. (3) gives

$$\epsilon_{\mathrm{eff}}(\omega)=\epsilon_B(\omega)\left\{\frac{1+2f_A[(\epsilon_A-\epsilon_B)/(\epsilon_A+2\epsilon_B)]}{1-f_A[(\epsilon_A-\epsilon_B)/(\epsilon_A+2\epsilon_B)]}\right\}, \tag{8}$$

which is asymmetric in $A$ and $B$.

The MG model corresponding to spherical air inclusions (material $A$) that are coated by SiC ($B$) is termed the cavity-Maxwell-Garnett model, and the reverse topology, that of SiC spheres ($A$) coated by air ($B$)—which is nonphysical—is the spherical-Maxwell-Garnett (S-MG) model; this is the same terminology as used in Ref. 1. Using the C-MG model with the effective dielectric function $\epsilon_A\equiv\epsilon_{\mathrm{air}}=1$ and $\epsilon_B\equiv\epsilon_{\mathrm{SiC}}(\omega)$,

$$\epsilon_{\mathrm{eff}}(\omega)=\frac{\epsilon_{\mathrm{SiC}}[2f(1-\epsilon_{\mathrm{SiC}})+(1+2\epsilon_{\mathrm{SiC}})]}{(1-f)+(2+f)\epsilon_{\mathrm{SiC}}}, \tag{9}$$

where $f$ $(=f_A)$ is the volume fraction of air (porosity).

The effective dielectric function for the S-MG model is

$$\epsilon_{\mathrm{eff}}(\omega)=\frac{2M(\epsilon_{\mathrm{SiC}}-1)+\epsilon_{\mathrm{SiC}}+2}{\epsilon_{\mathrm{SiC}}+2-M(\epsilon_{\mathrm{SiC}}-1)}, \tag{10}$$

where $M\equiv1-f_A$.

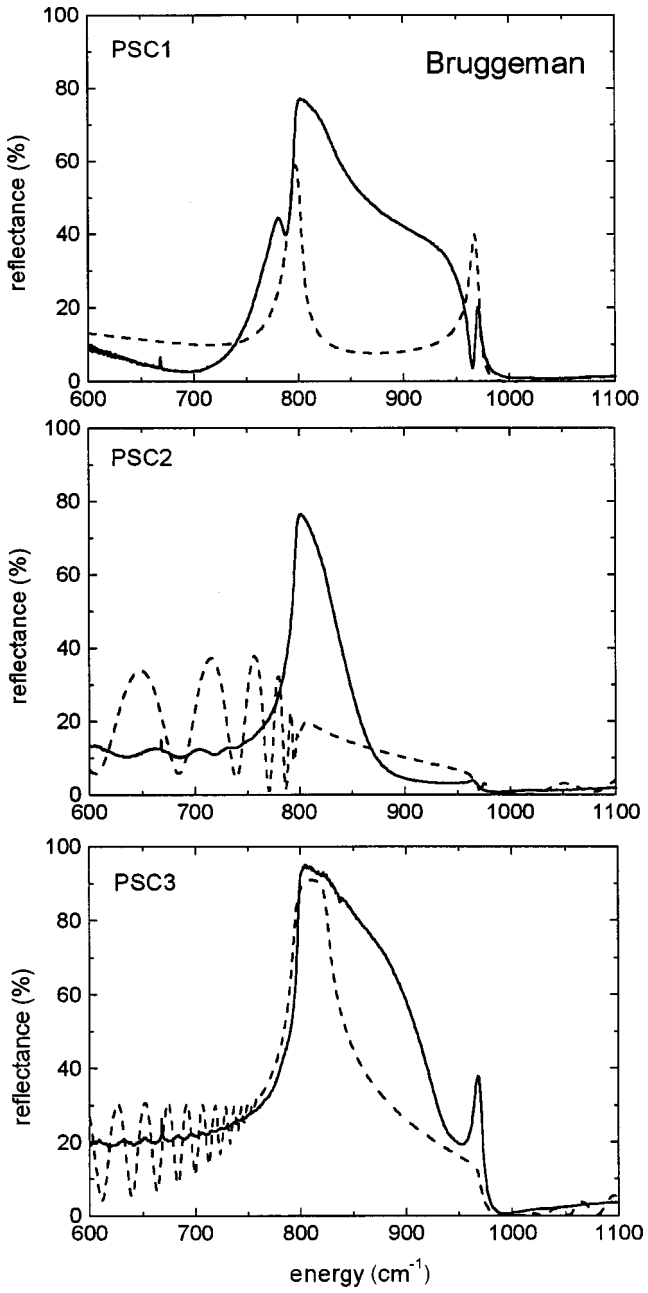


FIG. 2. Modeled unpolarized reflectance from PSC films on SiC substrates in the reststrahlen band using the Bruggeman model (dashed lines) for samples having thickness and porosity corresponding to the three PSC films; the measured reflectance is denoted by the solid lines.

Figures 3(a)–3(c) compare the simulated spectra (dashed lines) using the C-MG model with the measured spectra (solid lines). The model predicts a splitting of the reststrahlen band into a wide low-frequency band and a small, high-frequency band (located near 970 cm$^{-1}$), similar to what is observed. The LF band in the C-MG model is almost symmetric and boxlike, in contrast to the measured reflectance. (For $f=0.74$, this model predicts a minimum near 900 cm$^{-1}$ only for film thicknesses $0.1 \lesssim d \lesssim 10\ \mu$m and only for the *p*-polarized component.) The reverse topology (S-MG) model is even less successful (not shown). Aside from features caused by interference, the model reflectance is characterized by a broad band with a minimum near 910 cm$^{-1}$ for

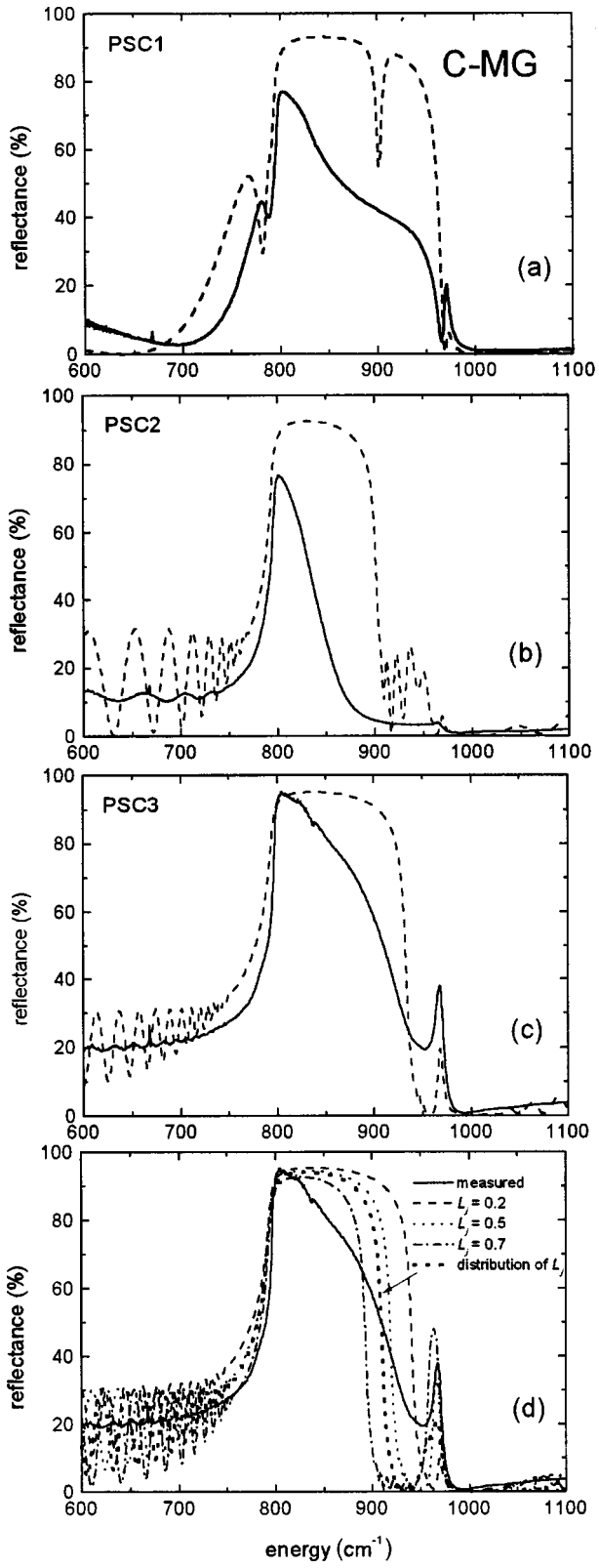


FIG. 3. Modeled reflectance from (a) PSC1, (b) PSC2, and (c) PSC3 films on SiC substrates using the cavity-Maxwell-Garnett (C-MG) model (dashed lines) for the three PSC films; the measured reflectance is denoted by the solid lines. (d) The same as (c), but using a modified C-MG model for spheroids with several depolarization factors $L_j$ and for a uniform distribution of $L_j$ from 0.01 to 0.99.

PSC1, two distinct peaks for both thick layers PSC2 and PSC3, and a single peak that rises near 900 $cm^{-1}$ for PSC3.

### C. Modifications to the cavity-Maxwell-Garnett and Bruggeman models

Porous silicon carbide consists of connected and elongated voids, and not the distinct spheres of air in the C-MG and Bruggeman models. Also, a large fraction of the PSC is at or near the surface of these voids, and the properties of these regions may be different from those of the bulk. Refinements of these effective-medium models are considered that reflect these features.

#### *1. Varying the void shape using a depolarization factor*

Under some preparation conditions, the pores in PSC preferentially grow perpendicular to the $(000\overline{1})$ surface, leading to ellipsoid-like or column-like voids; this may be due to enhanced field effects during the formation of porous semiconductor films.[18] The potential effect of pore shape on the dielectric function is examined by using an adjustable depolarization factor $L_j$ for ellipsoidal voids $(j=1,2,3)$. Equation (9) for the C-MG model is modified to give[19,20]

$$\epsilon_{\rm eff}(\omega)=\frac{f\epsilon_{\rm SiC}(1-\epsilon_{\rm SiC})(1-L_j)+\epsilon_{\rm SiC}[L_j+(1-L_j)\epsilon_{\rm SiC}]}{L_j+(1-L_j)\epsilon_{\rm SiC}-f(1-\epsilon_{\rm SiC})L_j}. \tag{11}$$

In SI units, $L_j=1/3$ for spherical cavities and $1/3<L_j<1$ for prolate spheroidal cavities (long axis along the normal to the layer and to the electric field).

Similarly, Eq. (6) for the Bruggeman model is generalized to

$$\left(\frac{\epsilon_1-\epsilon_{\rm eff}}{\epsilon_{\rm eff}+L_j(\epsilon_1-\epsilon_{\rm eff})}\right)f_1+\left(\frac{\epsilon_2-\epsilon_{\rm eff}}{\epsilon_{\rm eff}+L_j(\epsilon_2-\epsilon_{\rm eff})}\right)f_2=0. \tag{12}$$

Figure 3(d) shows the modeled reflectance corresponding to sample PSC3 using Eq. (11) for different depolarization factors (dashed lines) for the modified C-MG model, along with the measured spectra (solid line). Increasing $L_j$ increases the HF peak and narrows the LF peak, while maintaining the symmetry and vertical shoulders of the LF band. Overall, agreement with experiment is seen not to improve for this modified C-MG model or the modified Bruggeman model (not shown) when $L_j$ is varied. Also shown in the figure is the simulation for a uniform distribution of $L_j$ from 0.01 to 0.99. This distribution does not improve agreement with the observed spectra. Modifications to the S-MG model were not performed because of the poor results for the spherical crystallite model.

#### *2. A distinct surface layer: core-shell-medium model*

The damping characteristics of phonons on surfaces may be different from those of phonons inside the bulk of a material. Weaver *et al.*[21] and others[22] have recast the MG model to model a dielectric mixture consisting of three constituent materials, two of which are related. The topology is comprised of basic units of a core (unconnected spherical pores, for example) with given dielectric function $[\epsilon_c(\omega)]$, a surrounding shell with $[\epsilon_s(\omega)]$, and a surrounding medium $[\epsilon_m(\omega)]$. With this geometry and topology, the C-MG model can be modified to account for different phonon damping characteristics of the surface and the possibility of free-carrier absorption in the shell or medium. This model can also be used to include an oxide film on the pore walls, as was shown in Ref. 6.

The dielectric function for this three-component mixture is

$$\epsilon_{\rm eff}=\frac{f\epsilon_c A_c\rho^3+f\epsilon_s A_s(1-\rho^3)+\epsilon_m(1-f)}{fA_c\rho^3+fA_s(1-\rho^3)+1-f}, \tag{13}$$

where $A_c=3\epsilon_s B$, $A_s=(\epsilon_c+2\epsilon_s)B$, $\rho=r_c/r_s$, and

$$B=\frac{3\epsilon_m}{(\epsilon_s+2\epsilon_m)(2\epsilon_s+\epsilon_c)-2(\epsilon_s-\epsilon_m)(\epsilon_s-\epsilon_c)\rho^3}. \tag{14}$$

$r_c$ and $r_s$ are the radii of the core and shell, respectively, and $f$ is the total volume fraction of the cores and shells. Sasaki *et al.*[22] used the above model to describe the infrared absorption from small spherical SiC particles embedded in KBr by including a thin surface layer on the SiC spheres that possessed different phonon and plasmon damping characteristics.

The C-MG model is modified for PSC using this core-shell-medium (CSM) model. The core is taken as air ($\epsilon_c=1$), the surrounding medium as bulk SiC with $\epsilon_m=\epsilon_{\rm SiC}$, and the shell as a surface layer of SiC with $\epsilon_s=\epsilon_{\rm SiC\ surface}$. Equation (13) becomes

$$\epsilon_{\rm eff}=\frac{fA_c\rho^3+f\epsilon_{\rm SiC\ surface}A_s(1-\rho^3)+\epsilon_{\rm SiC}(1-f)}{fA_c\rho^3+fA_s(1-\rho^3)+1-f}, \tag{15}$$

where $A_c=3\epsilon_{\rm SiC\ surface}B$ and $A_s=(1+2\epsilon_{\rm SiC\ surface})B$. $\epsilon_{\rm SiC}$ is a Lorentzian [given by the first term in Eq. (1) with $\gamma=4.763\,{\rm cm}^{-1}$] and $\epsilon_{\rm SiC\ surface}$ described by Eq. (1), using both terms with variable plasma frequency $\omega_p$, and phonon ($\gamma$) and plasmon ($\Gamma$) damping rates. ''Coupling'' of the phonon and free-carrier terms can occur for large values of $\gamma$ and $\Gamma$. The modeled reflectance was studied as a function of shell (1) phonon damping rate, (2) plasma frequency and plasmon damping rate, and (3) thickness (relative to the pore radius). The volume fraction of air (the actual porosity) is $\rho^3 f$.

The inclusion of free-carrier absorption in the shell layer of SiC (with the same phonon damping parameter in the shell and medium) improves the agreement in the LF band, but eliminates the additional peak near 970 $cm^{-1}$ for all reasonable values of $\omega_p$ (750–4000 $cm^{-1}$) and $\Gamma$ (0–5000 $cm^{-1}$) (not shown). If the plasmon term is eliminated, so that the shell layer differs from the surrounding bulk only by its different phonon damping parameter $\gamma_{\rm shell}$, there are combinations of values for the two free parameters (e.g., $\gamma_{\rm shell}=150\,{\rm cm}^{-1}$ and $\rho=0.975$) for which there is reasonable agreement with the reflectance spectrum, as shown in Fig. 4. This damping width is much larger than that assumed in the bulk SiC, (4.763 $cm^{-1}$). Since it is likely that PSC is essentially depleted of free carriers, surface plasmon-phonon coupling should be insignificant here, as was concluded in earlier studies of porous GaAs.[23] It is unlikely that such surface effects are very important here.

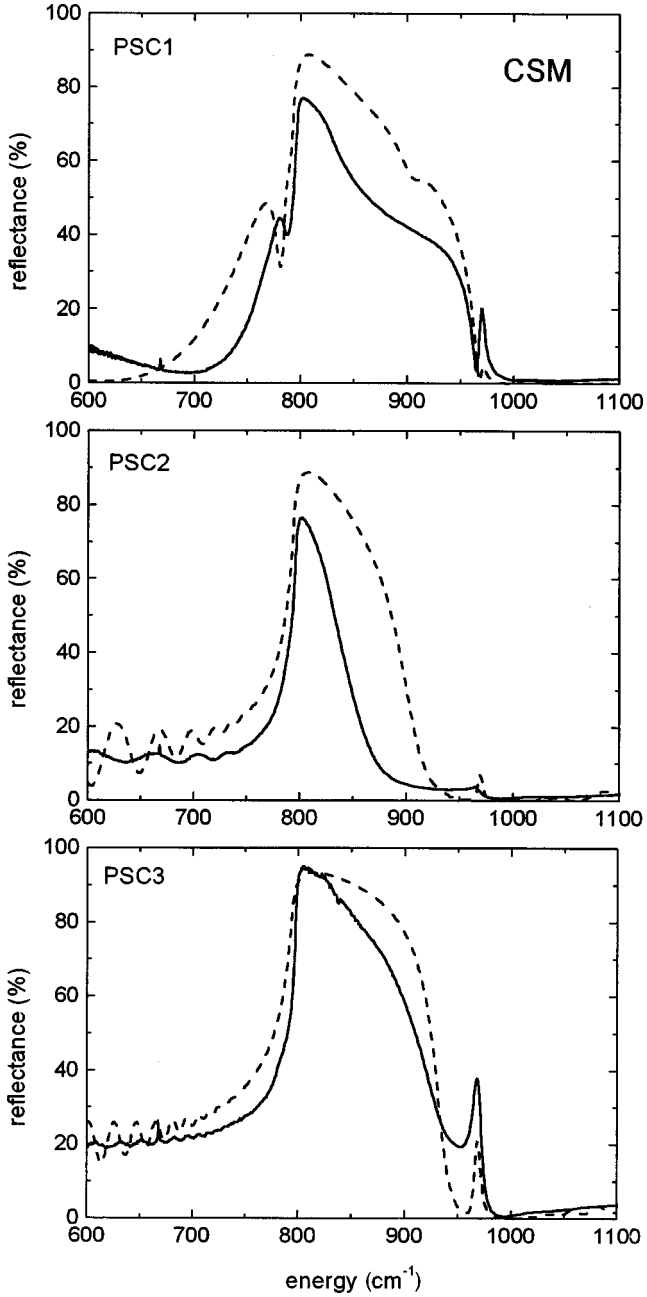


FIG. 4. Modeled reflectance from PSC films on SiC substrates using the core-shell-medium (CSM) variation of the C-MG model (dashed lines) for the three PSC films with $\gamma_{\text{shell}}=150\,\text{cm}^{-1}$, $\omega_{p,\text{shell}}=0$, $\Gamma_{\text{shell}}=0$, and $\rho=0.975$; the measured reflectance is denoted by the solid lines.

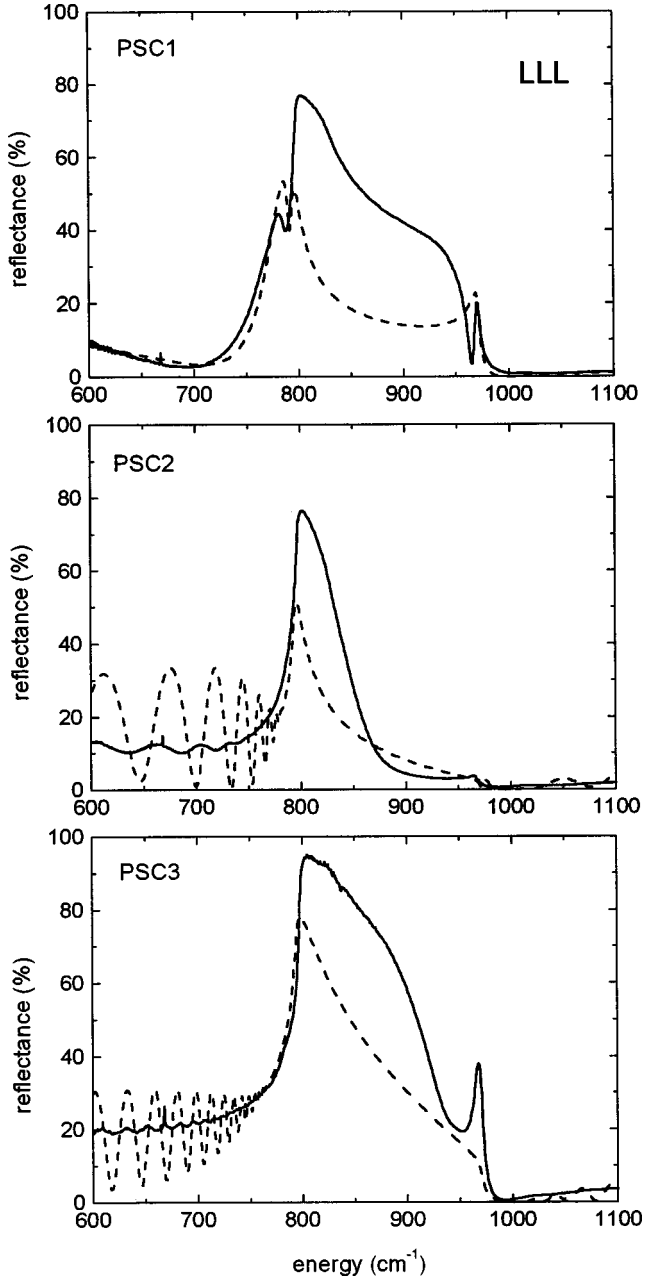


FIG. 5. Modeled reflectance from PSC films on SiC substrates using the Landau-Lifshitz/Looyenga (LLL) model (dashed lines) for the three PSC films; the measured reflectance is denoted by the solid lines.

### D. Landau-Lifshitz/Looyenga model

The effective-medium theory derived independently by Landau and Lifshitz[9] and Looyenga[10] has not been used previously to model PSC. Theiss[12] has shown that this model is more appropriate topologically for porous materials than are the Bruggeman and MG models. In LLL theory, a random, homogeneous, and isotropic mixture of two or more materials is assumed. Variations in the local field and local permittivity are small, the latter being small compared to the dielectric permittivity. The effective dielectric function is a weighted average of those for the constituents and is correct to the second order in the differences in the permittivities. For $N$ constituents,

$$\epsilon_{\text{eff}}^{1/3}=\langle \epsilon_i^{1/3}\rangle_{i=1}^{N}. \tag{16}$$

For two components with dielectric functions $\epsilon_1$ and $\epsilon_2$ and the volume fraction of component 2 called $f_2$,

$$\epsilon_{\text{eff}}=[(\epsilon_2^{1/3}-\epsilon_1^{1/3})f_2+\epsilon_1^{1/3}]^3. \tag{17}$$

Here, $\epsilon_1=\epsilon_{\text{SiC}}$ and $\epsilon_2=\epsilon_{\text{air}}=1$, and $f_2$ is the porosity of the film ($f$). Like the Bruggeman model, the LLL model is symmetric with respect to the two media. The LLL model results for the three samples are shown in Fig. 5 (dashed lines), along with the measured spectra

(solid lines). For the thin PSC film (PSC1), the LLL model produces a splitting of the band and the HF peaks that is also predicted by the C-MG model. However, there is essentially only a single peak (LF) with a sloping shoulder for the thick PSC films. The agreement with the measured spectra is slightly better than that using the Bruggeman model.

### E. Monecke model

The Monecke model is not based on a physical topology, but on an interpolation between the extreme limits of the mixture. For the case when it interpolates between the C-MG and S-MG models for spheres, the effective dielectric function is

$$\epsilon_{\rm eff}(\omega)=\frac{\epsilon_1[(\epsilon_2-\epsilon_1)/(2\epsilon_1+\epsilon_2)]+4(1-f)\epsilon_1+2(1-f)^2(\epsilon_2-\epsilon_1)}{[(\epsilon_2-\epsilon_1)/(2\epsilon_1+\epsilon_2)]+(1-f)}, \tag{18}$$

where $f$ is the porosity when $\epsilon_1$ is chosen to represent the dielectric function of air and $\epsilon_2$ that of the material. For the analogous case of aligned infinite cylinders whose axes are perpendicular to the electric field, the effective dielectric function is

$$\epsilon_{\rm eff}(\omega)=\epsilon_1\left(1-\frac{c-\eta}{s}-\frac{\eta}{s-s_0}\right), \tag{19}$$

where $s=\epsilon_1/(\epsilon_1-\epsilon_2)$, $\eta=(1/2s_0)f(1-f)$, and $s_0=1/2-(1-f)/2+3/2(1-f)^2-(1-f)^3$.

The simulations of the reststrahlen band in PSC using both Monecke models (not shown) are qualitatively similar to those with the C-MG model, and they do not agree any better with the measured spectra.

### F. Phenomenological hybrid models

The only simple phenomenological model that correctly predicts a distinct dip in the reststrahlen region *for all thicknesses* (including the infinite half-space of PSC) is the C-MG model. Still, the LLL model yields the shape of the HF shoulder of the LF band for thick PSC layers much better than the C-MG model. Thus, dielectric function models that include features of both of these models are considered. One hybrid dielectric function model uses the LLL mixing rule, Eq. (17),

$$\epsilon_{\rm eff}(\omega)=[(1-\epsilon_{\rm CMG}^{1/3})f_{\rm LLL}+\epsilon_{\rm CMG}^{1/3}]^3, \tag{20}$$

to mix the C-MG medium ($\epsilon_{\rm CMG}$)

$$\epsilon_{\rm CMG}(\omega)=\frac{\epsilon_{\rm SiC}[2f_{\rm CMG}(1-\epsilon_{\rm SiC})+(1+2\epsilon_{\rm SiC})]}{(1-f_{\rm CMG})+(2+f_{\rm CMG})\epsilon_{\rm SiC}} \tag{21}$$

with air. The total porosity is

$$f_{\rm total}=f_{\rm LLL}+f_{\rm CMG}(1-f_{\rm LLL}). \tag{22}$$

If $f_{\rm total}$ is known and $f_{\rm CMG}$ ($\leqslant f_{\rm total}$) is selected, $f_{\rm LLL}$ is determined. At the limits, the original C-MG model with a topology of spherical cavities of air corresponds to $f_{\rm LLL}=0$, and the LLL completely random mixture corresponds to $f_{\rm CMG}=0$.

Setting the measured porosity equal to $f_{\rm total}$ and varying $f_{\rm CMG}$, agreement of this CMG-in-LLL hybrid model is poor for thin PSC and is good for the thicker PSC films, as shown in Fig. 6. Decreasing $f_{\rm CMG}$ lowers the peak reflectance near $\omega_T$.

Alternatively, a hybrid dielectric function can be constructed using the C-MG mixing rule, Eq. (9), with porosity $f_{\rm CMG}$ to mix the LLL medium with porosity $f_{\rm LLL}$ described by Eq. (17). Now the total porosity is

$$f_{\rm total}=f_{\rm CMG}+f_{\rm LLL}(1-f_{\rm CMG}). \tag{22'}$$

Figure 7 shows that agreement for this LLL-in-CMG hybrid model is again poor for thin PSC and somewhat better for thick PSC films. $f_{\rm LLL}=0.4$ gives a good fit for PSC2 and $f_{\rm LLL}=0.15$ gives a good fit for PSC3.

The LLL model describes an isotropic mixture whose constituent phases are not spatially correlated; i.e., the mixture is completely random (there is no interfacial surface). The first CMG-in-LLL hybrid model physically consists of a random LLL mixture of two media, each of which has an imposed local spatial correlation by virtue of defining the two constituents to be (1) PSC, represented as air cavities surrounded by bulk SiC with the C-MG form of the dielectric function [Eq. (21)], and (2) air itself. The geometrical arrangement of pores (air) neither is completely fixed as discrete cavities (C-MG) nor is the air mixed with the SiC in a completely random way (LLL). A much higher volume fraction (of air in the present case) can be used here than would be rigorously valid for the C-MG model alone. The local structure of the PSC in this hybrid model is represented by small cavities of air (C-MG), while the longer-range structure is random (LLL). The second LLL-in-CMG hybrid model consists of the random LLL media with discrete air cavities (C-MG).

### G. Statistical hybrid model using the Bergman representation

The generalized statistical formulation of the dielectric function of a mixture developed by Bergman[16] has been applied extensively by Theiss[12] and others.[15] The effective dielectric function for a mixture of two materials having complex, frequency-dependent dielectric functions $\epsilon_A(\omega)$ and $\epsilon_B(\omega)$ can be written as

$$\epsilon_{\rm eff}(\omega)=\epsilon_A(\omega)\left(1-f_B\int_0^1\frac{g(n)}{t(\omega)-n}dn\right), \tag{23}$$

where

$$t(\omega)=\frac{\epsilon_A(\omega)}{\epsilon_A(\omega)-\epsilon_B(\omega)} \tag{24}$$

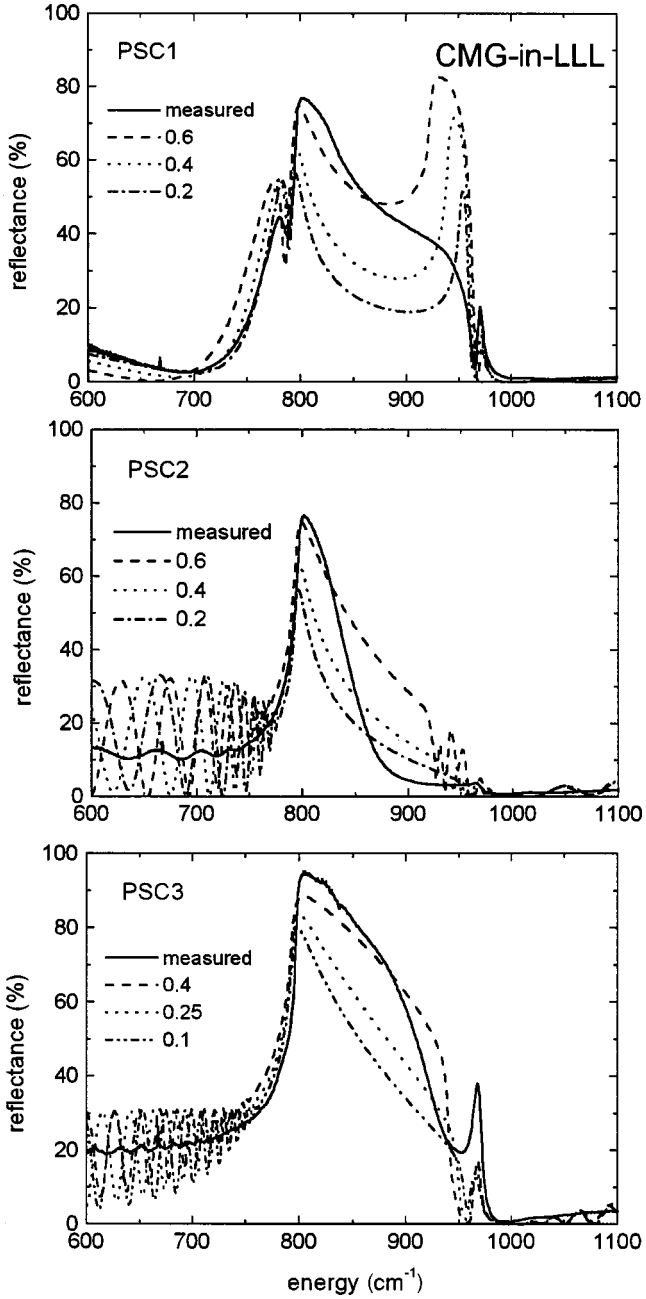


FIG. 6. Modeled reflectance from PSC films on SiC substrates using the phenomenological CMG-in-LLL hybrid model for selected values of $f_{\mathrm{CMG}}$ for total porosity $f=0.74$, 0.74, and 0.5 corresponding to the three PSC films; the measured reflectance is denoted by the solid lines.

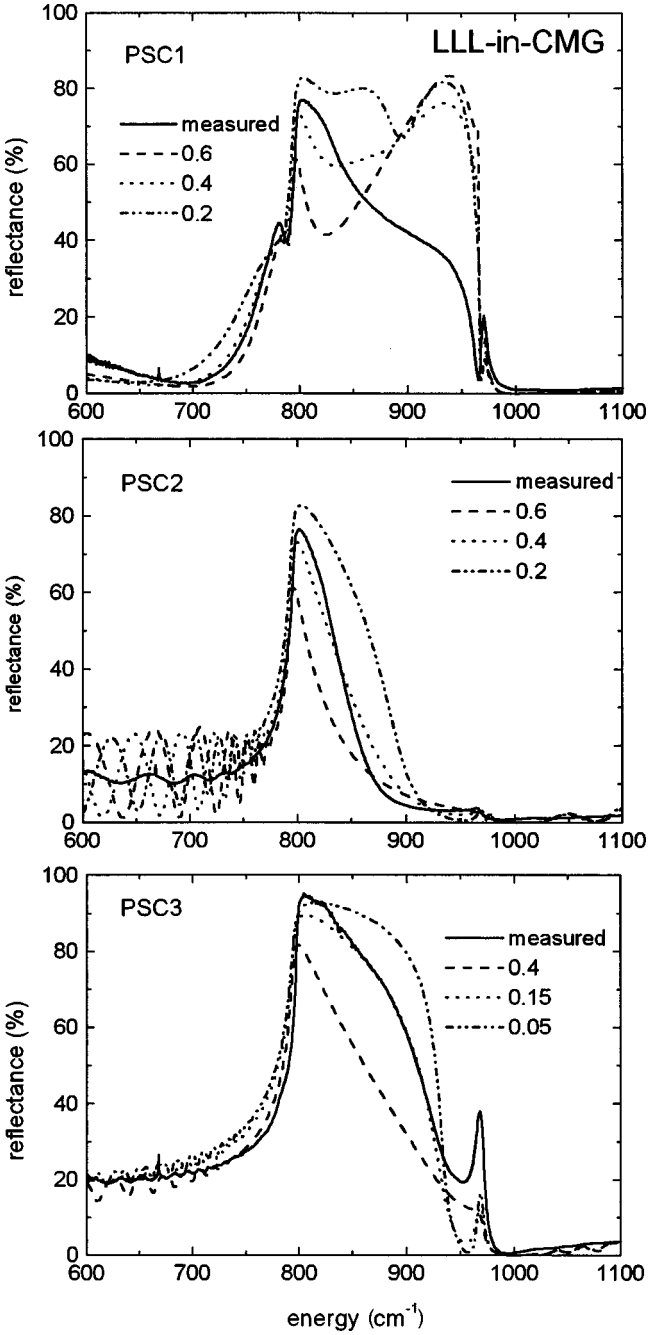


FIG. 7. Modeled reflectance from PSC films on SiC substrates using the phenomenological LLL-in-CMG hybrid model for selected values of $f_{\mathrm{CMG}}$ for total porosity $f=0.74$, 0.74, and 0.5 corresponding to the three PSC films; the measured reflectance is denoted by the solid lines.

is the reduced dielectric function, $f_B$ is the volume fraction of material $B$, $n$ is the depolarization factor, and $g(n)$ is the spectral density function, which is also a function of the porosity. $g(n)$ is a single-valued, real function that depends only on the topology and volume fraction, and has a well-defined analytic form for the cases of the simple effective-medium formulas. This function is subject to the condition of normalization (uniformity of the topology) for a porous material

$$\int_0^1 g(n)dn=1 \tag{25}$$

and, for statistically isotropic mixtures, the moment rule

$$\int_0^1 ng(n)dn=(1-f_B)/3. \tag{26}$$

For PSC, SiC will be called material $A$ and air (vacuum) material $B$ so that $f_B$ is the porosity.

Large resonances occur in Eq. (23) when the real part of $\epsilon_{\mathrm{eff}}$ falls below zero so the integrand diverges, corresponding to values of $0\leqslant t(\omega)\leqslant 1$. This range corresponds to a region of frequencies over which the dielectric function and the re-

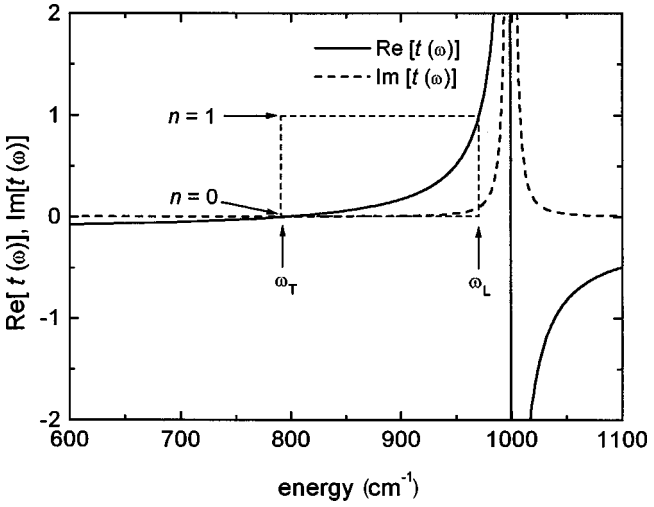


FIG. 8. Real (solid line) and imaginary (dashed line) parts of reduced dielectric function $t(\omega)$ of SiC in air, demonstrating the spectral region over which the dielectric function is sensitive to topology.

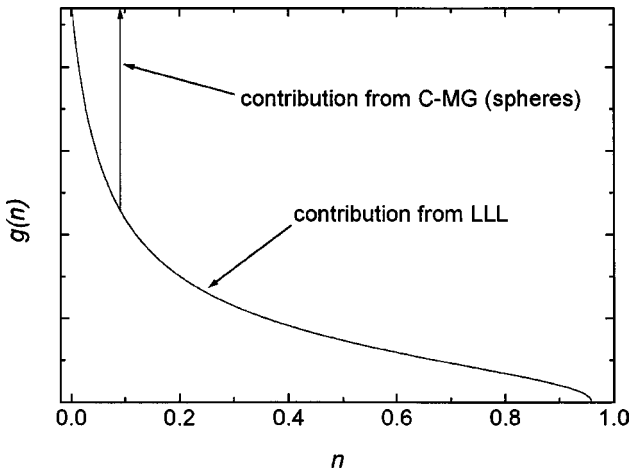


FIG. 9. Plot of hybrid spectral density $g(n)$ as a function of depolarization factor $n$ for linear mixing of the C-MG and LLL models with mixing parameter $\alpha=0.5$. The C-MG model component is a Dirac function. The LLL model portion also has a Dirac $\delta$ function component at $n=0$.

flectance are expected to be sensitive to the topology. Figure 8 plots the real and imaginary parts of $t(\omega)$; it is seen that this resonance condition is met in the spectral region of the reststrahlen band.

In principle, the topology function $g(n)$ could be determined numerically from the experimentally determined $\epsilon_{\text{eff}}$. In practice, however, Eq. (23) is a Fredholm integral equation of the first kind, ill posed, and therefore it is unstable upon inversion. This means that small errors in $\epsilon_{\text{eff}}$ correspond to enormous errors in the determination of $g(n)$. Instead, a Monte Carlo–like algorithm has been applied to determine a unique $g(n)$ that optimizes agreement with experimental data.[25] A different approach is followed here. The spectral density functions of the simple phenomenological models are combined to produce a hybrid statistical model. In principle, this offers the possibility of combining the features of any number of phenomenological models into the statistical theory to give a model with a direct physical interpretation. This approach can also be used to generate a reasonable initial guess for a more exact determination of $g(n)$ by nonlinear regression; this is not done here.

The dielectric mixture of PSC is represented here by a linear combination of the LLL and C-MG spectral density functions. The LLL and C-MG models each predict different features in the measured spectra. The normalized spectral densities characterizing the LLL and C-MG models are, respectively,[25]

$$g_{\text{LLL}}=f^2\delta_+(n)+\frac{3\sqrt{3}}{2\pi}\left((1-f)^2\left|\frac{n-1}{n}\right|^{1/3}+f(1-f)\left|\frac{n-1}{n}\right|^{2/3}\right)(1-\delta_{0,n}) \tag{27}$$

and

$$g_{\text{CMG}}=\delta\left(n-\frac{1-f}{3}\right). \tag{28}$$

The linear combination of these two relations has $\alpha$ as the only free parameter:

$$g_{\text{hybrid}}(n)\equiv\alpha g_{\text{CMG}}(n)+(1-\alpha)g_{\text{LLL}}(n). \tag{29}$$

This spectral density $g_{\text{hybrid}}(n)$ automatically satisfies Eqs. (25) and (26) and is shown for $\alpha=0.5$ in Fig. 9. Figure 10 shows the modeled reflectance with this Bergman model (simulation denoted by the dashed lines and measured reflectance by the solid lines). This model agrees better with the measured spectra than any other model considered. The optimum value of $\alpha$ is 0.5 for PSC1, 0.5 for PSC2, and 0.7 for PSC3. The variation in model simulation with $\alpha$ is seen for PSC3 in Fig. 10, where results for $\alpha=0.3$, 0.5, and 0.7 are plotted. Even though $\alpha=0.7$ is optimal for PSC3, $\alpha=0.5$ still gives a relatively good fit.

### H. Porosity depth gradients

Porosity changes with depth can occur during the fabrication of porous layers from gradients in the ion concentration over an increasingly thick porous layer, progressive chemical etching of the upper portion of the porous layer, and the trapping of dissolved or undissolved gas inside the porous network (which may inhibit charge transfer locally). The problem of porosity gradients is potentially more severe in $n$-PSC formed by light-assisted anodization, using $h\nu \geqslant E_g$, due to gradients in the absorption of the illumination. Thönissen *et al.*[26] have discussed the nature and origins of the porosity gradients that are present in porous silicon, and have given recipes[27] for the real-time adjustment of the anodic current to prevent or reduce these gradients. Porosity variations across the thickness of the PSC film can affect the infrared reflectance and the determination of the mean-field dielectric function. Porosity gradients were modeled here with an optical matrix approach[28] using the C-MG, Bruggeman, and LLL effective-medium theories; these simulations do not agree substantially better than those in which the porosity does not change with depth.

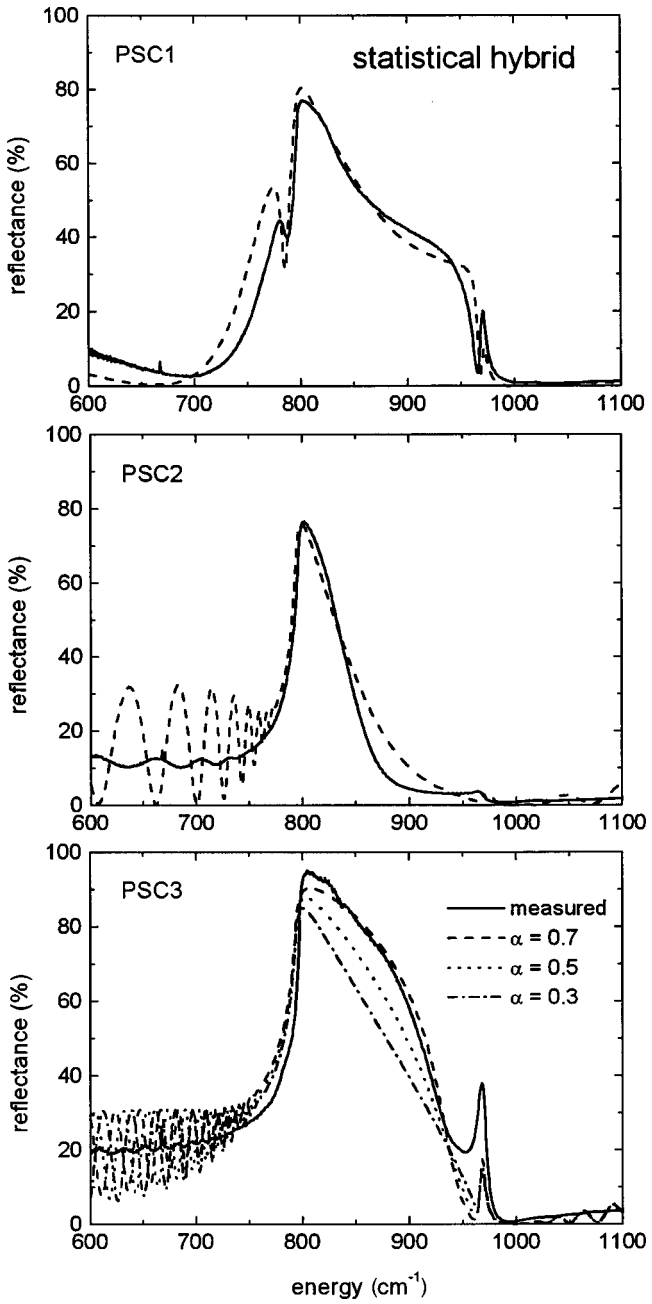


FIG. 10. Modeled reflectance from PSC films on SiC substrates using the Bergman statistical hybrid model with $\alpha=0.5$ (dashed lines) for the three PSC films; the measured reflectance is denoted by the solid lines. For comparison, model fits for $\alpha=0.3$ and 0.7 and are also shown for PSC3.

Furthermore, a model of a porous layer on a bulk substrate should include the effects of roughness, particularly at the porous-bulk interface. The roughness at the PSC/SiC interface decreases the specular reflectance by a factor of $\exp[-(4\pi\sigma/\lambda)^2]$.[29] $\sigma$ is the rms value of the roughness and $\lambda$ is the wavelength. This roughness is estimated to be no larger than 50 nm on the basis of cross-section SEM. $\sigma=50$ nm is used here, which is also consistent with published values for the porous Si/bulk Si interface with the same substrate doping type, similar doping concentration,[30] and similar pore and crystallite sizes[2] as used here. Within the reststrahlen band, this roughness decreases the reflectance by no more than 0.3%, and has little effect on the analysis here. This loss increases with energy, from $\sim$ 0.6% to 6% over the range 1200 to 4000 $cm^{-1}$[Fig. 1(b)].

## V. DISCUSSION

### A. Performance of the effective-medium models

None of the simple phenomenological models adequately describes (1) the splitting of the reststrahlen band into a broad primary peak (LF band) and a sharp HF peak, separated by the dip, and (2) the gradual slope of the high-frequency shoulder of the LF band; the agreement is especially poor for the thin PSC layer. The C-MG and Monecke models are the only ones that produce a somewhat symmetric LF band and the dip for all thicknesses above 0.25 $\mu$m (for $f=0.74$), but they predict a fairly symmetrical LF band. The LLL, and to a limited extent, the Bruggeman models exhibit the gradual slope of the HF shoulder of the LF peak, but these produce the HF peak only for very thin layers.

The MG model for a binary system is strictly valid in the limit of a small concentration of one of the constituent materials, namely, $\lesssim 0.15$.[17] It is not rigorously correct to apply any of the MG-based models for a wide range of porosities, as was shown in Ref. 1, including the range here, $0.5\leqslant f \leqslant 0.74$. The S-MG geometry of separated spherical SiC particles corresponds to a physically impossible topology. The inclusion of the effects of varying void shape did not result in any substantial improvement of the modeled reflectance. The inclusion of an additional surface layer with higher phonon damping in the CSM modification of the C-MG model did lead to an improvement in the modeled reflectance, but only with the freedom of two adjustable parameters.

The simpler LLL model fails to describe the splitting of the reststrahlen band for moderate to large values of PSC film thickness, but at least qualitatively predicts the asymmetry of the LF band. This latter feature may be attributed to the completely random, homogeneous, and isotropic nature of this mixture. The LLL model is rigorously valid for all values of volume fraction because it represents a mixture whose constituent materials are percolated at all volume fractions.

Hybridization of the LLL and C-MG models whether phenomenologically or directly statistically gives the best representation of the dielectric function. Still, the statistical hybrid is clearly superior to both phenomenological versions for all samples studied. The statistical hybrid model spectral density gives good initial values for $g(n)$ from which even better spectral density functions can be determined.

One beneficial feature of the statistical theory is the applicability of the spectral density function $g(n)$ as a topology function of a given mixture from which other topologically sensitive transport properties, including thermal conductivity, frequency-dependent electrical conductivity, and diffusivity, can be determined. In principle, analysis of nondestructive and noncontact infrared (or optical) reflection of a dielectric mixture film with a statistical effective dielectric function can provide not only an improved description of the topology, but these other properties as well. Note that Theiss[12] has shown that $\epsilon_{\text{eff}}$ must be determined for a range of conditions (porosity, topology, etc.), whatever the effective-medium theory, to prove that the model is valid

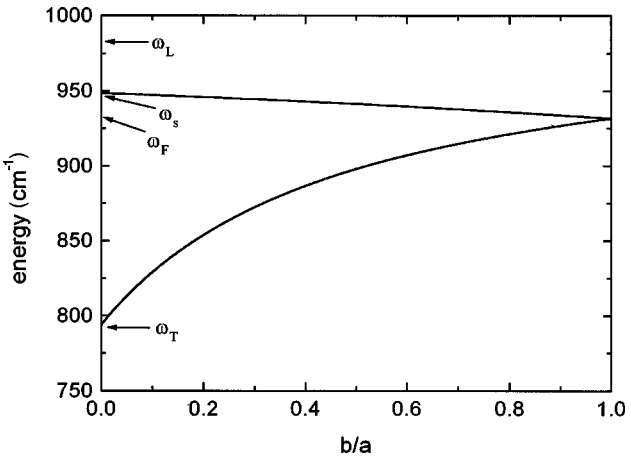


FIG. 11. Fundamental mode frequencies for SiC prolate spheroids as the ratio of the minor to major axis ($b/a$) varies from 0 (cylinder, $L=0$ and $\frac{1}{2}$) to 1 (sphere, $L=\frac{1}{3}$).

over the full range of parameter space; comparison of model and experiment for only one sample is not sufficient.

### B. Physical origin of the splitting of the reststrahlen band

While the dielectric functions from the statistical model implicitly include the mesoscopic phenomena that cause the splitting of the reststrahlen band in PSC, a more explicit identification of the phenomena is desired. Surface optical phonon modes in polar semiconductors are known to exist in the reststrahlen region from $\omega_T$ (794 cm$^{-1}$) to $\omega_L$(970 cm$^{-1}$), where Re($\epsilon$)$<$0. These have been shown to cause changes in the reststrahlen band of rough surfaces, such as on $\beta$-SiC layers.[31,32] Surface optical phonons have been observed in the Raman scattering from porous GaAs Ref. 23 and porous GaP,[24] and should also strongly affect the IR spectrum of porous materials.

For SiC ellipsoids in air that are much smaller than a wavelength of the probing light, the frequencies of these surface modes can often be expressed as[33]

$$\epsilon_{\mathrm{SiC}}(\omega_i) = -\alpha_i \epsilon_{\mathrm{air}}. \tag{30}$$

For the fundamental (lowest-order) modes

$$\alpha_j = \left(\frac{A}{L_j} - 1\right), \tag{31}$$

where $L_j$ are the three polarization factors ($j=1,2,3$) and $A=1$ in SI units and $4\pi$ in cgs units. For spheres, the modes have $\alpha_n=(n+1)/n$ where $n=1,2,3,\ldots$ is the mode order. The lowest-order mode is the Fröhlich mode $\alpha_1=2$ ($\omega_F=932\,\mathrm{cm}^{-1}$ for SiC) and the higher-order modes converge to $\alpha_\infty=1$ ($\omega_s=949\,\mathrm{cm}^{-1}$); the surface mode series converges to $\omega_s$ for any crystal shape. The Fröhlich mode splits into two modes as the sphere is deformed into a spheroid ($L_1=L_2\neq L_3$); for prolate spheroids approaching a cylinder, these frequencies approach $\omega_T$ (794 cm$^{-1}$, $L=0$) and $\omega_s$ (949 cm$^{-1}$, $L=1/2$). This is seen in Fig. 11. Both modes are usually important in reflection. For oblate spheroids approaching a slab, these frequencies approach $\omega_T$ (794 cm$^{-1}$, $L=0$) and $\omega_L$ (970 cm$^{-1}$, $L=1$).

Since the SiC network in PSC roughly resembles interconnected prolate ellipsoids of a range of shapes and orientations, the dip in the reststrahlen band in PSC can be attributed to a range of surface optical phonon modes. The minimum of the dip is seen in the range $\sim$ 940 to 965 cm$^{-1}$. The dip is asymmetric, changing more gradually at lower energy and more sharply at higher energy near $\omega_L$. This is consistent with a range of ellipsoidal geometries, as can be seen for the specialized case of prolate spheroids in Fig. 11, because the density of frequencies from $\omega_F$ to $\omega_s$ (932–949 cm$^{-1}$) is higher than that from $\omega_F$ to $\omega_T$ (932–794 cm$^{-1}$).

The spectral density spectrum $g(n)$ in Eq. (23) has been identified as being equivalent to the surface phonon mode spectrum.[12] This is seen in the close connection between the resonance condition in the statistical representation with the reduced dielectric function $t(\omega)$ between $n=0$ and 1, and the surface phonon mode spectra. Note that Eq. (24) is identical to Eq. (30) with Eq. (31), when $L_j$ is replaced by $t(\omega)$.

Coupling of surface phonons and plasmons has been seen in nanocrystals.[34–36] However, there is evidence that this coupling may not occur in porous materials[24] because of charge depletion in the porous skeleton. The plasmon term in Eq. (1) does not seem to be important in most of the models considered here.

Figure 3(d) shows the C-MG model with aligned spheroids of a specific polarization factor, and for a range of polarization factors. This last curve is different from this proposed explanation in that it assumes air cavities with those cavities aligned in a specific direction. Note that Ref. 1 suggested that the structure in the reststrahlen band can be attributed to the polarization associated with an air cavity resonance at 959 cm$^{-1}$.

It is possible that the observed dip in the unpolarized reflectance may be due to the Berreman effect.[37] The Berreman effect is the observation of absorption in the reststrahlen band in the *p*-polarized reflectance at oblique angles of incidence for thin films of an ionic crystal with thickness less than a wavelength or for thin films on conducting substrates. The Berreman effect was originally observed in thin, insulating layers on metallic, highly conductive substrates, but has been demonstrated recently in homoepitaxial 6H-SiC in which the carrier concentration in the epilayer is low compared to that in the substrate.[38] Since the observed dip in the reststrahlen band occurs even for very thick porous layers ($\sim$50 $\mu$m) and for near-normal incidence, it is not likely that the Berreman effect is significant here.

### C. Comparison of the spectral density functions of the hybrid models

Both the ''phenomenological'' and ''statistical'' hybrid models have an adjustable parameter in addition to the porosity *f*, i.e., $f_{\mathrm{CMG}}$ (or $f_{\mathrm{LLL}}$) and $\alpha$, respectively. The statistical model seems fine for all the cases studied, while both hybrid phenomenological models are good for the thicker films, but poor for the thin film.

The differences in how the media are mixed in these hybrid models can be seen by comparing their spectral density functions. That for the ''statistical'' hybrid, shown in Fig. 9, retains the percolation property of the LLL model with a

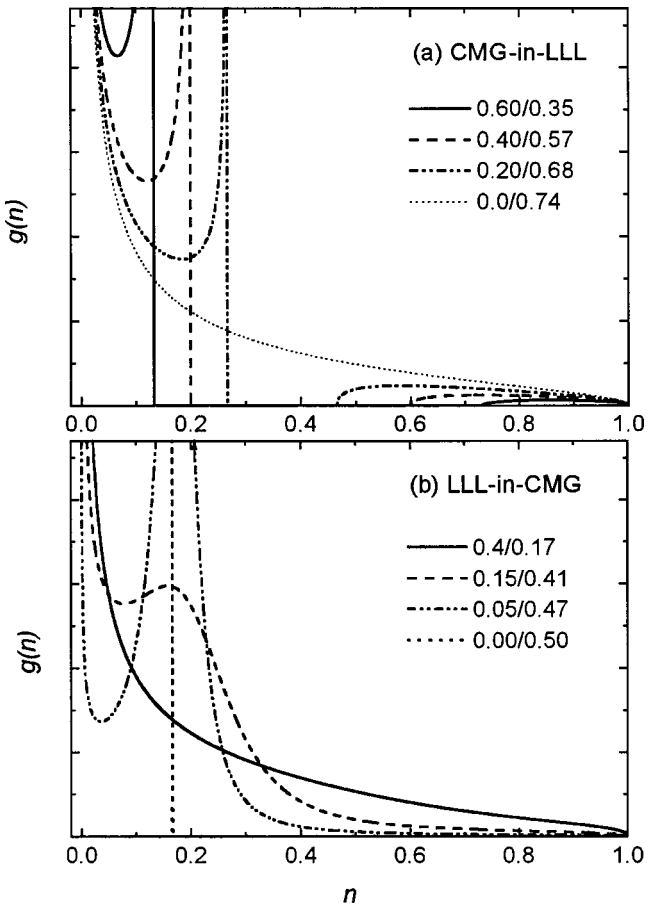


FIG. 12. The spectral density $g(n)$ for (a) the CMG-in-LLL hybrid, phenomenological model for $f_{\text{total}}=0.74$ and selected paired values of $f_{\text{CMG}}/f_{\text{LLL}}$ and (b) the LLL-in-CMG hybrid, phenomenological model for $f_{\text{total}}=0.50$ and selected paired values of $f_{\text{LLL}}/f_{\text{CMG}}$.

continuous, nonzero spectrum of $g(n)$ for all $n$; this is equivalent to saying that it includes contributions from all possible surface phonon modes (Fig. 11). This percolation property seems to make it suitable for representing porous materials.[12] $g(n)$ also has the Dirac $\delta$ function of the C-MG model.

The spectral density functions for the phenomenological hybrid models are determined by defining $G(\omega)$ using Eq. (23) and the relation[12]

$$\epsilon_{\text{eff}}(\omega)=\epsilon_A(\omega)[1-G(\omega)] \tag{32}$$

and then using it in

$$g(n)=-\frac{1}{2\pi i f_{\text{total}}}\lim_{\beta\to 0}[G(n+i\beta)-G(n-i\beta)]. \tag{33}$$

Using Eq. (20) for $\epsilon_{\text{eff}}$ in the CMG-in-LLL model gives a $g(n)$ that is plotted in Fig. 12(a) for several representative parameters, along with the pure LLL model. The mixing defined by Eqs. (20) and (21) seems to lead to an interference between the LLL and C-MG features of $g(n)$. $g(n)$ retains much of the C-MG Dirac $\delta$ function character and some, but not all, of the LLL character. It asymptotically approaches $g(n)$ for the LLL model as $n$ approaches 0 and 1. $g(n)$ is now zero over stretches of the $n=0$ to 1 range, for example, from 0.13 to 0.73 for $f_{\text{LLL}}=0.60$, from 0.20 to 0.60 for $f_{\text{LLL}}=0.40$, and from 0.27 to 0.47 for $f_{\text{LLL}}=0.20$. Therefore this hybrid CMG-in-LLL ''phenomenological'' model may not be ideal for porous materials.

The spectral density function of the LLL-in-CMG hybrid phenomenological model is qualitatively different. Figure 12(b) shows that the continuous nature of $g(n)$ of the LLL model, which is needed to describe the percolation feature of porous materials, is always seen here. This is reasonable since the material phase is always continuous and is always locally a medium described by the LLL model. The C-MG Dirac $\delta$ function feature monotonically broadens as $f_{\text{CMG}}$ decreases and $f_{\text{LLL}}$ increases for a fixed $f_{\text{total}}$.

## VI. CONCLUSIONS

The effective-medium model of PSC derived from a linear combination of the spectral distribution functions for the C-MG and LLL phenomenological models leads to spectra simulations that are in very good agreement with the observed IR reflectance spectra of PSC films in the reststrahlen band. It is superior to the phenomenological-based C -MC/LLL hybrid models and is far superior to the simple phenomenological models. The splitting of the reststrahlen band is PSG predicted by the statistical model is attributed to a wide spectrum of surface optical phonons. This statistical treatment gives information about the topology in porous materials and can help predict topologically sensitive transport properties.

## ACKNOWLEDGMENTS

The authors gratefully acknowledge the assistance of Dr. Luis Avila of the Department of Chemistry at Columbia, and support from the Joint Services Electronics Program (JSEP) under Contract No. DAA-G-55-97-1-0166, the MRSEC Program of the National Science Foundation under Grant No. DMR-9809687, and Kulite Semiconductor Products, Inc., Leonia, NJ.

## APPENDIX: OPTICAL MODEL OF THE PSC/SiC STRUCTURE

The PSC layer is treated as an isotropic layer of thickness $d$ and complex index of refraction $n_{\text{PSC}}(\omega)$ (medium 2) below the ambient layer $(n=1)$ (medium 1) and on a semi-infinite bulk substrate of SiC (medium 3). The SiC is modeled as a uniaxial medium with its optical axis ($c$ axis) oriented perpendicular to the PSC/bulk interface. (It is uncertain if PSC is less anisotropic than SiC. In any case, estimates show that assuming PSC to be isotropic affects the spectral simulation very little.)

The diagonalized dielectric tensor $\epsilon_{ij}$ for SiC has two unique nonzero elements, $\epsilon_{33}=\epsilon_{\perp}=n_{\perp}^2$ (parallel to the optic, or $c$ axis, and perpendicular to the 0001 plane) and $\epsilon_{11}$ $(=\epsilon_{22})=\epsilon_{\parallel}=n_{\parallel}^2$ (parallel to the basal plane). $\epsilon_{\perp}$ and $\epsilon_{\parallel}$ are each expressed as Lorentzian oscillators [Eq. (1), with $\epsilon_{\infty\perp}$ $=6.52$ and $\epsilon_{\infty\parallel}=6.70$].[39]

For a wave incident at an angle $\theta_i$, the reflection coefficients from this structure are calculated for $s$ (perpendicular) and $p$ (parallel) polarizations,

$$\tilde{r}_{123s,p}=\frac{\tilde{r}_{12s,p}+\tilde{r}_{23s,p}e^{i\beta}}{1+\tilde{r}_{12s,p}\tilde{r}_{23s,p}e^{i\beta}}, \tag{A1}$$

where $\tilde{r}_{12s,p}$ and $\tilde{r}_{23s,p}$ are the reflection coefficients for the air-PSC and PSC–bulk SiC interfaces, respectively, and

$$\tilde{\beta}=\frac{2\pi}{\lambda}(2d\sqrt{\tilde{n}_2^2-\sin^2\theta_i}). \tag{A2}$$

The boundary conditions are the continuity of the tangential components of the $E$ and $H$ fields at each interface.

At the air-PSC interface

$$\tilde{r}_{12,s}=\frac{\cos\theta_i-(n_{\mathrm{PSC}}^2-\sin^2\theta_i)^{1/2}}{\cos\theta_i+(n_{\mathrm{PSC}}^2-\sin^2\theta_i)^{1/2}} \tag{A3}$$

and

$$\tilde{r}_{12,p}=\frac{n_{\mathrm{PSC}}^2\cos\theta_i-(n_{\mathrm{PSC}}^2-\sin^2\theta_i)^{1/2}}{n_{\mathrm{PSC}}^2\cos\theta_i+(n_{\mathrm{PSC}}^2-\sin^2\theta_i)^{1/2}}. \tag{A4}$$

At the PSC/SiC interface for $s$ polarization (the ordinary wave),[40]

$$\tilde{r}_{23,s}=\frac{(n_{\mathrm{PSC}}^2-\sin^2\theta_i)^{1/2}-(n_{\perp}^2-\sin^2\theta_i)^{1/2}}{(n_{\mathrm{PSC}}^2-\sin^2\theta_i)^{1/2}+(n_{\perp}^2-\sin^2\theta_i)^{1/2}}. \tag{A5}$$

For $p$ polarization (the extraordinary wave),

$$\tilde{r}_{23,p}=\frac{n_{\parallel}n_{\perp}(n_{\mathrm{PSC}}^2-\sin^2\theta_i)^{1/2}-n_{\mathrm{PSC}}^2(\epsilon_{\parallel}n_{\mathrm{PSC}}^2-\sin^2\theta_i)^{1/2}}{n_{\parallel}n_{\perp}(n_{\mathrm{PSC}}^2-\sin^2\theta_i)^{1/2}+n_{\mathrm{PSC}}^2(\epsilon_{\parallel}n_{\mathrm{PSC}}^2-\sin^2\theta_i)^{1/2}}. \tag{A6}$$

Substituting Eqs. (A3) and (A5), or Eqs. (A4) and (A6), into Eq. (A1) gives the reflection coefficient. The reflectance for the three-layer system is $R_{123s,p}(\omega)=|\tilde{r}_{123s,p}(\omega)|^2$. The unpolarized reflectance is the average of the reflectance due to incident $s$ and $p$ components of equal intensity.


[1] M. F. MacMillan, R. P. Devaty, W. J. Choyke, J. E. Spanier, D. Goldstein, and A. D. Kurtz, J. Appl. Phys. **80**, 2412 (1996).

[2] J. E. Spanier, G. S. Cargill III, I. P. Herman, S. Kim, D. R. Goldstein, A. D. Kurtz, and B. Z. Weiss, in *Advances in Microcrystalline and Nanocrystalline Semiconductors*, edited by R. W. Collins, P. M. Fauchet, I. Shimizu, J.-C. Vial, T. Shimada, and A. P. Alivisatos, MRS Symposia Proceedings No. 452 (Materials Research Society, Pittsburgh, 1997), p. 491.

[3] H. Mimura, T. Matsumoto, and Y. Kanemitsu, Appl. Phys. Lett. **65**, 3350 (1994).

[4] V. B. Shields, M. A. Ryan, R. M. Williams, M. G. Spencer, D. M. Collins, and D. Zhang, in Silicon Carbide and Related Materials, 1995, edited by S. Nakashima, H. Matsunami, S. Yoshida, and H. Harima, No. 142 (Institute of Physics, London, 1996), IOP Conf. Proc. Chap. 7, p. 1067.

[5] J. E. Spanier and I. P. Herman, in *Materials and Devices for Silicon-based Optoelectronics*, edited by A. Polman, S. Cofta, and R. Soref, MRS Symposia Proceedings No. 486 (Materials Research Society, Pittsburgh, 1998), p. 317.

[6] J. E. Spanier and I. P. Herman, J. Porous Mater. **7**, 139 (2000).

[7] J. E. Spanier and I. P. Herman (unpublished).

[8] D. A. G. Bruggeman, Ann. Phys. (Leipzig) **24**, 636 (1935).

[9] L. D. Landau and E. M. Lifshitz, *Electrodynamcis of Continuous Media*, 2nd ed. (Butterworth-Heinenann, Oxford, 1984), p. 42.

[10] H. Looyenga, Physica (Amsterdam) **31**, 401 (1965).

[11] I. Mihalcescu, G. Lerondel, and R. Romestain, Thin Solid Films **297**, 245 (1997).

[12] W. Theiss, Adv. Solid State Phys. **33**, 149 (1994).

[13] W. G. Spitzer, D. A. Kleinman, and D. Walsh, Phys. Rev. **113**, 127 (1959).

[14] J. C. Maxwell Garnett, Philos. Trans. R. Soc. London, Ser. A **203**, 385 (1904).

[15] J. Monecke, J. Phys.: Condens. Matter **6**, 907 (1994); Phys. Status Solidi B **155**, 437 (1989); **154**, 805 (1989).

[16] D. J. Bergman, Phys. Rep., Phys. Lett. **43C**, 377 (1977).

[17] I. Webman, J. Jortner, and M. H. Cohen, Phys. Rev. B **15**, 5712 (1977).

[18] M. I. J. Beale, J. D. Benjamin, M. J. Ulren, N. G. Chew, and A. G. Cullis, J. Cryst. Growth **73**, 622 (1985).

[19] R. W. Cohen, G. D. Cody, M. D. Coutts, and B. Abeles, Phys. Rev. B **8**, 3689 (1973).

[20] G. A. Niklasson and C. G. Granqvist, J. Appl. Phys. **55**, 3382 (1984).

[21] J. H. Weaver, R. W. Alexander, L. Teng, R. A. Mann, and R. J. Bell, Phys. Status Solidi A **20**, 321 (1973).

[22] Y. Sasaki, Y. Nishina, M. Sato, and K. Okamura, Phys. Rev. B **40**, 1762 (1989).

[23] I. M. Tiginyanu, G. Irmer, J. Monecke, A. Vogt, and H. L. Hartnagel, Semicond. Sci. Technol. **12**, 491 (1997).

[24] I. M. Tiginyanu, G. Irmer, J. Monecke, and H. L. Hartnagel, Phys. Rev. B **55**, 6739 (1997).

[25] J. Sturm, P. Grosse, and W. Theiss, Z. Phys. B: Condens. Matter **83**, 361 (1991).

[26] M. Thönissen, S. Billat, M. Krüger, H. Lüth, M. G. Berger, U. Frochter, and U. Rossow, J. Appl. Phys. **80**, 2990 (1996).

[27] M. Thönissen, M. G. Berger, W. Theiss, S. Hilbrich, M. Krüger, R. Arens-Fischer, S. Billat, G. Lerondel, and H. Lüth, in *Advances in Microcrystalline and Nanocrystalline Semiconductors* (Ref. 2), p. 431.

[28] M. Born and E. Wolf, *Principles of Optics*, 6th ed. (Pergamon, Oxford, 1980).

[29] H. E. Bennett and J. O. Porteus, J. Opt. Soc. Am. **51**, 123 (1961).

[30] G. Lérondel, R. Romestain, and S. Barret, J. Appl. Phys. **81**, 6171 (1997).

[31] V. Hopfe, W. Grählert, K. Brennfleck, E. H. Korte, and W. Theiss, Fresenius J. Anal. Chem. **346**, 99 (1993).

[32] R. T. Holm, P. H. Klein, and P. E. R. Nordquist, Jr., J. Appl. Phys. **60**, 1479 (1986).

[33] R. Ruppin, Surf. Sci. **35**, 20 (1973).

[34] K. H. Reider, M. Ishigame, and L. Genzel, Phys. Rev. B **6**, 3804 (1972).

[35] R. Ruppin and J. Nahum, J. Phys. Chem. Solids **35**, 1311 (1974).

[36] K. Yamamoto, K. Kimura, M. Ueda, H. Kasahara, and T. Okada, J. Phys. C **18**, 2361 (1985).
[37] D. W. Berreman, Phys. Rev. **130**, 2193 (1963).
[38] S. Zollner, J. P. Carrejo, T. E. Tiewald, and J. A. Woollam, Phys. Status Solidi B **208**, R3 (1998).
[39] L. Patrick and W. Choyke, Phys. Rev. B **2**, 2255 (1970).
[40] L. P. Mosteller, Jr., and F. Wooten, J. Opt. Soc. Am. **58**, 511 (1968).